

Covalency in Metal–Oxygen Multiple Bonds Evaluated Using Oxygen K-edge Spectroscopy and Electronic Structure Theory

Stefan G. Minasian,^{†,‡} Jason M. Keith,[†] Enrique R. Batista,^{†,*} Kevin S. Boland,[†] Joseph A. Bradley,[§] Scott R. Daly,[†] Stosh A. Kozimor,^{*,†} Wayne W. Lukens,[‡] Richard L. Martin,^{†,*} Dennis Nordlund,[⊥] Gerald T. Seidler,^{||} David K. Shuh,^{‡,*} Dimosthenis Sokaras,[⊥] Tolek Tyliczszak,[‡] Gregory L. Wagner,[†] Tsu-Chen Weng,[⊥] and Ping Yang[#]

[†]Los Alamos National Laboratory, Los Alamos, New Mexico 87545, United States

[‡]Lawrence Berkeley National Laboratory, Berkeley, California 94720, United States

[§]Lawrence Livermore National Laboratory, Livermore, California 94550, United States

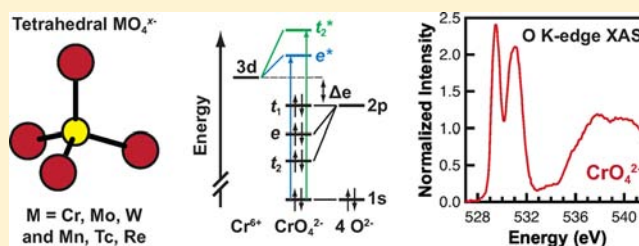
[⊥]SLAC National Accelerator Laboratory, Menlo Park, California 94025, United States

^{||}University of Washington, Seattle, Washington 98195, United States

[#]Pacific Northwest National Laboratory, Richland, Washington 99352, United States

Supporting Information

ABSTRACT: Advancing theories of how metal–oxygen bonding influences metal oxo properties can expose new avenues for innovation in materials science, catalysis, and biochemistry. Historically, spectroscopic analyses of the transition metal MO_4^{x-} anions have formed the basis for new M–O bonding theories. Herein, relative changes in M–O orbital mixing in MO_4^{2-} ($M = \text{Cr, Mo, W}$) and MO_4^- ($M = \text{Mn, Tc, Re}$) are evaluated for the first time by nonresonant inelastic X-ray scattering, X-ray absorption spectroscopy using fluorescence and transmission (via a scanning transmission X-ray microscope), and time-dependent density functional theory. The results suggest that moving from Group 6 to Group 7 or down the triads increases M–O e^* (π^*) mixing; for example, it more than doubles in ReO_4^- relative to CrO_4^{2-} . Mixing in the t_2^* orbitals ($\sigma^* + \pi^*$) remains relatively constant within the same Group, but increases on moving from Group 6 to Group 7. These unexpected changes in orbital energy and composition for formally isoelectronic tetraoxometalates are evaluated in terms of periodic trends in d orbital energy and radial extension.



INTRODUCTION

The nature of chemical bonds between metals and light atoms such as oxygen, nitrogen, and carbon is of widespread interest because these interactions control the physics and chemistry of many technologically important processes and compounds. Light atoms are prone to form highly covalent metal–ligand multiple bonds involving one σ bond and one or more π bonds, resulting in oxo, imido, nitrido, alkylidene, alkylidyne, and carbido functionalities with many desirable chemical reactivities and physical properties.¹ Among this diverse group, metal oxides stand out because of their widespread presence in biological and bio-inspired processes and for applications utilizing their unique magnetic, electronic, and thermal properties.^{2–14} Ligand field theory and concepts including the “oxo wall” have successfully predicted the relative stabilities of many tetragonal compounds and catalysts containing metal monooxo or dioxo bonds.^{15–23} Developing a clear understanding of how M–O electronic structure and orbital mixing changes for a range of metal oxo compounds and materials will greatly benefit attempts to advance technologies that incorporate metal oxides.

Among approaches explored previously, ligand K-edge X-ray absorption spectroscopy (XAS) has emerged as an effective method for quantitatively probing electronic structure and orbital mixing in metal–chlorine and metal–sulfur bonds.²⁴ This spectroscopic technique probes bound state transitions between core ligand 1s orbitals and unoccupied molecular orbitals. The excitations can only have transition intensity if the empty acceptor orbitals contain ligand p character.²⁴ At first glance, such an approach seems well-suited for studying metal–oxygen bonding. However, attempts to use this technique to study nonconducting molecular systems are complicated by experimental barriers derived from the low energy of the oxygen K-edge (ca. 530 eV), which magnifies issues associated with surface contamination, saturation, and self-absorption effects.

In this manuscript, we overcome these challenges and evaluate relative changes in metal–oxo electronic structure and orbital mixing for nonconducting molecular solids using O K-

Received: October 23, 2012

Published: January 28, 2013

edge spectroscopy in conjunction with hybrid density functional theory (DFT) calculations. Specifically, nonresonant inelastic X-ray scattering (NIXS), XAS, and time-dependent density functional theory (TD-DFT) are used as complementary techniques to assess bonding in the MO_4^{2-} ($M = \text{Cr}, \text{Mo}, \text{W}$) and MO_4^- ($M = \text{Mn}, \text{Tc}, \text{Re}$) anions.²⁵ These highly symmetric d^0 metal oxides were selected as analytes because historically they were foundational in development of valence bond theory for tetrahedral compounds.^{26,27} Developing the chemistry of these MO_4^{x-} anions is also needed to support a variety of applications, which include use as stoichiometric and catalytic oxidants,^{14,28,29} in radiopharmaceutical purifications,³⁰ and in advanced nuclear fuel separations.³¹ Despite the similarities of these isoelectronic d^0 MO_4^{2-} and MO_4^- anions, we find significant differences in σ - and π -type metal oxo orbital mixing both for adjacent metals in the same row as well as for metals within the same group triad. The combined experimental and theoretical study is consistent with well-established models of bonding, however, theory and experiment diverge in some notable instances.

RESULTS AND DISCUSSION

Ground-State Electronic Structure Calculations. Oxygen K-edge spectroscopy probes bound-state dipole-allowed transitions of O 1s electrons into vacant molecular orbitals that contain O 2p character due to metal–oxygen orbital mixing.³² Before presenting the experimental results, it is instructive to discuss the electronic structure calculations that guided spectral interpretations. Because the electronic structures for T_d - MO_4^{x-} are well-established,^{27,33} this discussion focuses on the unoccupied metal-based orbitals relevant to the O K-edge spectra. Results from the DFT calculations are consistent with group theory, and can be summarized as follows. A symmetry-adapted linear combination (SALC) of the four oxygen 2p atomic orbitals having σ -symmetry with respect to the M–O bond spans $a_1 + t_2$ symmetries. The remaining eight oxygen 2p SALCs have π -symmetry with respect to the M–O bond and span $e + t_1 + t_2$ symmetries. With this designation, metal s, p, and d orbitals are allowed by symmetry to form M–O σ -interactions of a_1 and t_2 symmetry and π -interactions of t_2 and e symmetry, which leaves the O 2p orbitals of t_1 symmetry as nonbonding oxygen lone pairs (HOMO). Overall, this provides two sets of unoccupied e^* (π^* ; LUMO) and t_2^* ($\sigma^* + \pi^*$; LUMO+1) orbitals that primarily contain metal d character and is consistent with established bonding pictures for tetrahedral compounds (Figure 1).

Density functional theory calculations using relativistic effective core potentials (RECPs) were conducted to determine how antibonding molecular orbital compositions and energies varied as (1) metals changed within a group (Cr, Mo, W and Mn, Tc, Re) and (2) nuclear charges of the metal increased from Group 6 to Group 7, which is accompanied by a decrease in anionic charge from MO_4^{2-} to MO_4^- . The molecular orbital picture determined by DFT (Figure 2 and Table S1 in the Supporting Information) is consistent with conclusions from group theory. As expected based on the relative energies of the 3d, 4d, and 5d atomic orbitals, an increase in energy for the e^* and t_2^* orbitals was observed within a group triad, such that $\text{Cr} < \text{Mo} < \text{W}$ and $\text{Mn} < \text{Tc} < \text{Re}$ (Figure 2). These orbitals also decrease in energy on moving from Group 6 (MO_4^{2-}) to Group 7 (MO_4^-), e.g., $\text{Cr} > \text{Mn}$ and $\text{Mo} > \text{Tc}$. Participation of the O 2p orbitals in the e^* and t_2^* orbitals is calculated to decrease subtly with heavier metals in an individual Group triad

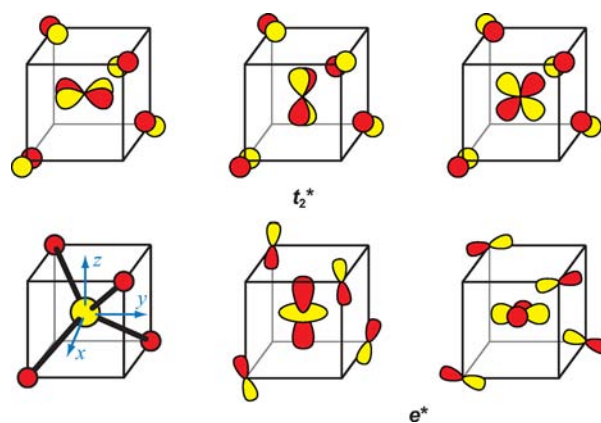


Figure 1. Antibonding interaction of metal d orbitals with the oxygen e and t_2 orbitals.

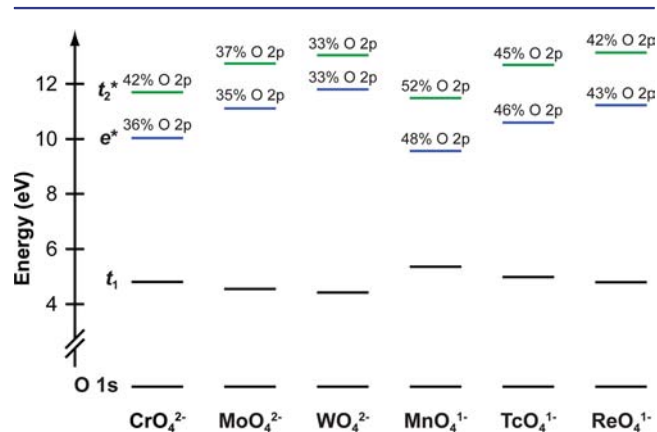


Figure 2. Correlation of the calculated molecular orbital diagrams for d^0 MO_4^{x-} anions showing the t_1 HOMO (black) and virtual orbitals of e (blue) and t_2 (green) symmetry. Molecular orbitals energies are based on the data in Table S1 (Supporting Information), but have been shifted by a constant so that the O 1s orbitals all have energies of -508.4 eV.

as shown by the decrease in oxygen 2p character (Figure 2). More profound changes in oxygen 2p character are calculated on moving from Group 6 to Group 7, which is also correlated with an increase in the nuclear charge on the metal. For example, the O 2p character for the ReO_4^- e^* and t_2^* orbitals (43.2 and 41.8%, respectively) is appreciably larger than that observed for the same orbitals on WO_4^{2-} (33.2 and 32.6%).

O K-Edge Spectra. Oxygen K-edge spectra for the MO_4^{2-} ($M = \text{Cr}, \text{Mo}, \text{W}$) and MO_4^- ($M = \text{Mn}, \text{Tc}, \text{Re}$) anions were obtained using a variety of excitation sources and detection methods to ensure that accurate representations of the O K-edge data were obtained, and to characterize contributions from radiation damage, saturation, self-absorption, and surface contamination.³² To demonstrate that correct O K-edge data have been acquired, Figure 3 shows the background-subtracted and normalized O K-edge NIXS spectra for Na_2CrO_4 , Na_2MoO_4 , and Na_2WO_4 and the O K-edge XAS obtained in transmission mode using a scanning transmission X-ray microscope (STXM) and by fluorescence yield (FY) detection. Each spectrum contains two large pre-edge features indicative of covalent M–O bonding between ca. 525 and 535 eV. To a first approximation, these pre-edge features correspond to transitions from O 1s orbitals to unoccupied molecular orbitals formed by interactions between O 2p and metal d orbitals, as

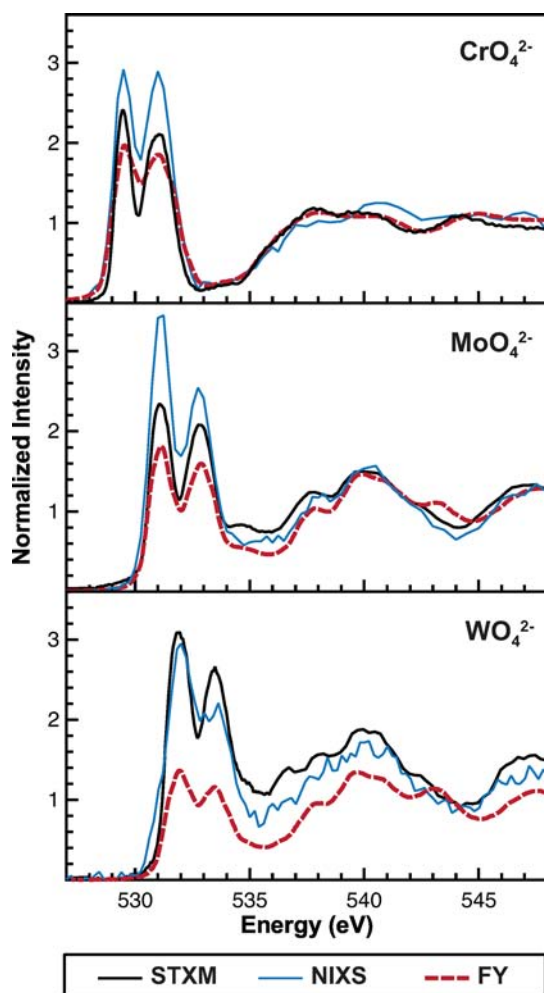


Figure 3. O K-edge XAS of the Group 6 CrO_4^{2-} , MoO_4^{2-} , and WO_4^{2-} anions. Spectra shown were measured in X-ray transmission (STXM, black trace), scattering (NIXS, blue trace), and fluorescence (FY, dashed red trace) detection modes.

described above. Moving down a row to heavier metals—i.e., from Cr to Mo to W—causes both pre-edge peaks to shift to higher energies (Table 1). Analogous increases in pre-edge peak energy have been observed previously in the Cl and S K-edge XAS of transition metal coordination compounds, and were attributed to the increasing energy of the 3d, 4d, and 5d atomic orbitals.^{36–40}

Group 7 d^0 KMnO_4 , $(\text{Ph}_4\text{P})\text{TcO}_4$, and NaReO_4 salts were analyzed to evaluate how traversing from left to right in the periodic table affected the O K-edge MO_4^{x-} spectra (Supporting Information). Not all measurements could be performed on KMnO_4 or $(\text{Ph}_4\text{P})\text{TcO}_4$ owing to the susceptibility of KMnO_4 toward radiation damage and difficulties associated with handling radioactive ^{99}Tc . Spectra for NaReO_4 have been provided in an earlier publication.³² Because analyses on Na^+ , K^+ , and Ph_4P^+ salts of ReO_4^- provided equivalent data, within experimental error, we assume that pre-edge spectral contributions from O–Na and O–K interactions are not appreciable.

The O K-edge NIXS and XAS spectra for the MO_4^- and MO_4^{2-} salts were modeled as described previously using symmetrically constrained Gaussian line shapes and a step function with a 1:1 ratio of arctangent and error function contributions.³² Curve-fitting models of the XAS (trans-

Table 1. Comparison of Experimental and Calculated O K-edge Pre-edge Peak Energies (eV) and Intensities (Int)^a for MO_4^{x-} (M = Cr, Mn, Mo, Tc, W, Re; x = 1, 2)

method	$1s \rightarrow e^*$		$1s \rightarrow t_2^*$		splitting eV	ratio ^b Int
	eV	Int	eV	Int		
CrO_4^{2-}						
TD-DFT	529.5	2.9	531.0	3.4	1.5	0.9
FY	529.5	1.7(1)	531.1	3.1(2)	1.6	0.5
STXM	529.5	1.9(2)	531.0	3.4(3)	1.5	0.6
NIXS	529.5	2.9(3)	531.0	4.5(4)	1.6	0.7
MnO_4^-						
TD-DFT	528.8	3.7	530.5	4.3	1.7	0.9
FY	528.9	1.9(1)	530.5	3.9(2)	1.5	0.5
STXM	528.8	2.9(3)	530.3	5.3(5)	1.5	0.6
MoO_4^{2-}						
TD-DFT	531.1	3.5	532.8	3.2	1.7	1.1
FY	531.1	2.2(1)	532.9	2.7(1)	1.8	0.8
STXM	531.1	2.7(3)	532.8	3.2(3)	1.7	0.8
NIXS	531.1	4.0(4)	532.8	3.8(4)	1.7	1.0
TcO_4^-						
TD-DFT	530.4	4.0	532.4	3.9	2.0	1.0
STXM	530.4	3.1(3)	532.3	4.4(4)	1.9	0.7
WO_4^{2-}						
TD-DFT	531.9	3.9	533.4	2.7	1.5	1.4
FY	531.9	1.8(1)	533.5	1.7(1)	1.6	1.1
STXM	531.9	3.9(4)	533.5	3.6(4)	1.6	1.1
NIXS	531.9	4.0(4)	533.5	3.6(4)	1.6	1.1
ReO_4^-						
TD-DFT	531.4	4.2	533.4	3.7	2.0	1.1
FY	531.4	3.2(2)	533.6	4.4(2)	2.2	0.7
STXM	531.4	4.2(4)	533.7	5.7(6)	2.3	0.7
NIXS	531.4	5.0(5)	533.5	6.9(7)	2.1	0.7

^aThe TD-DFT calculated energies and intensities were adjusted based on the experimental data (see Experimental Section). ^bRatios are equal to the $1s \rightarrow e^*$ intensity divided by the $1s \rightarrow t_2^*$ intensity.

mission) data are shown in Figure 4 and Table 1 (see Supporting Information for NIXS and FY models). In each case the analyses agreed well with the experimental data as shown by low correlation coefficients, residual data that only slightly deviated from a line of zero intensity, and symmetric residual peaks that were similar in shape to the parent Gaussian functions (see Supporting Information). Errors associated with the area (hereafter referred to as the intensity) of the low-energy curve-fitting functions due to normalization or curve-fitting were estimated at 5% for the FY data and 10% for the STXM and NIXS data.³² Each spectrum, whether it was obtained using NIXS, STXM, or FY, also exhibited an additional third feature in the low-intensity valley after the two main pre-edge features and before the onset of the rising edge. The close proximity of these features to the rising edge results in greater uncertainty in the intensity of their corresponding curve-fit functions; consequently, only the intensities for the first two most intense features are discussed.

The two intense features at low energy in each O K-edge spectrum were well-resolved from the rising edge and intensities were determined with confidence from the area of the corresponding curve-fit functions. As noted previously,³² accurate comparisons between pre-edge intensities can be derived from both NIXS and transmission data because contributions from self-absorption and saturation effects are not present (NIXS)^{41–43} or can be minimized/eliminated

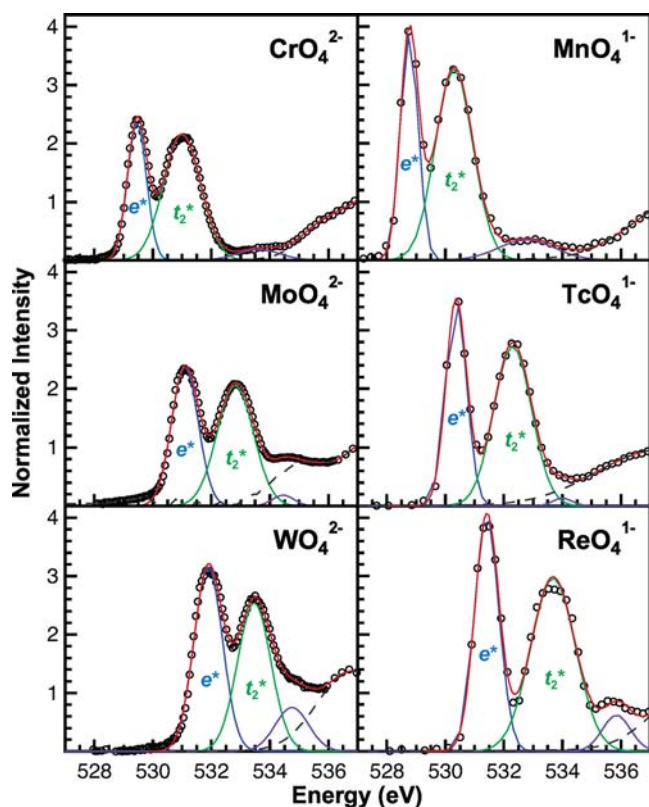


Figure 4. O K-edge XAS (STXM) experimental data (black circles), Gaussian functions (blue, green, and purple traces) used to generate the curve-fits (red traces), and post-edge residual data (dashed gray traces).

(STXM).⁴⁴ In contrast, FY measurements provide reduced spectral intensities due to saturation and/or self-absorption effects, stemming from the relative size of the particles compared to characteristic X-ray penetration lengths ($\sim 1 \mu\text{m}$) and high concentrations of analyte required for the measurement. Hence, comparisons between NIXS and STXM data for MO_4^{2-} and MO_4^{-} show that pre-edge peak positions decrease in energy from Group 6 to Group 7 (Mn < Cr, Tc < Mo and Re < W), which is accompanied by an increase in pre-edge peak intensities measured for the Group 7 (MO_4^{-}) compounds relative to Group 6 (MO_4^{2-}). Origins for these changes in spectral intensity are discussed below.

Spectral Interpretations. Calculated O K-edge spectra were generated using time-dependent DFT (TD-DFT) to guide spectral interpretations (Figure 5 and Table 1). This approach has been applied successfully to simulate spectra for several other transition metal systems^{37,38,45–47} and to simulate the absorption spectrum of MnO_4^{-} .⁴⁸ Each calculated spectrum has been shifted by approximately +13 eV to account for omission of electronic relaxation and other effects (see Experimental Section).^{49,50} Absolute energies and peak splittings for the first two features in the O K-edge spectra measured using NIXS and obtained by XAS (STXM and FY) all agree with the TD-DFT simulated values (Table 1). The TD-DFT calculations are also consistent with expectations from group theory, which show that the only spin and dipole allowed transitions for each of the $d^0 \text{MO}_4^{x-}$ complexes must be between $^1A_1 \rightarrow ^1T_2$ states. Hence, the first pre-edge feature in each of the O K-edge spectra is assigned to an excitation from the O 1s ligand orbitals of t_2 symmetry to the e^* molecular

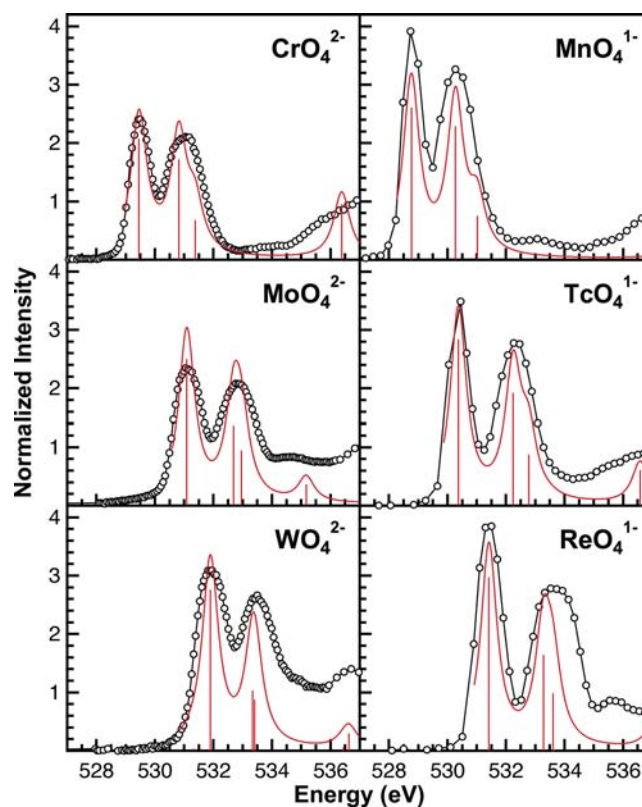


Figure 5. O K-edge XAS (STXM) experimental data (black circles), the TD-DFT calculated spectra (red traces), and calculated transitions (red bars).

orbitals, while the second feature consists of closely spaced excitations from O 1s orbitals of a_1 and t_2 symmetry to the t_2^* orbitals (Figure 5 and Table 1). As expected based on the DFT calculated e^* and t_2^* orbital energies, both transitions decrease in energy from group 6 to group 7 (Mn < Cr, Tc < Mo, Re < W). The O $1s \rightarrow e^*$ and O $1s \rightarrow t_2^*$ transitions also increase in energy by 1.6 to 2.0 eV on moving from row IV to row V metals and 0.6 to 1.1 eV on moving from row V to row VI metals. Additional confidence in this spectral interpretation is obtained by comparing the O K-edge XAS with published UV-visible spectra.²⁷ Figure 6 depicts this graphically by showing the linear relationship between the O $1s \rightarrow e^*$ ($^1A_1 \rightarrow ^1T_2$) O K-edge excitation energies and the HOMO $\rightarrow e^*$ ($^1A_1 \rightarrow ^1T_2$) UV-visible excitation energies.

The calculations also predict transitions that may account for the third low intensity and high-energy feature in the experimental spectra (see above). Consistent with our earlier report describing the NaReO_4 O K-edge spectrum,³² and similar to several other ligand K-edge studies,^{46,51–53} the electronic structure calculations on MO_4^{2-} and MO_4^{-} attribute this high-energy feature to transitions involving higher lying Rydberg-type orbitals. These allowed transitions involve electronic states that result from small amounts of mixing between the higher lying metal orbitals (e.g., 4p for CrO_4^{2-}) and O p orbitals. The DFT results suggest that these orbitals are not associated with the antibonding counterpart of any occupied bonding orbitals; hence, the minor amount of transition intensity observed for the third feature is not likely to be indicative of ground-state bond covalency.

Evaluating M–O Orbital Mixing. Relative changes in the O K-edge transition intensities can be used to quantify the

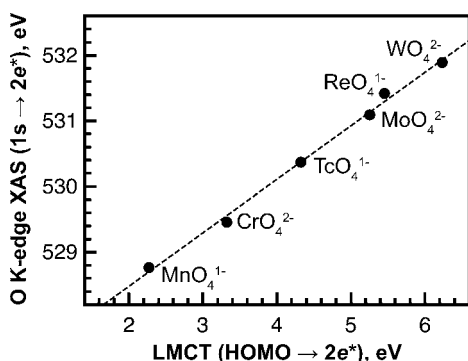


Figure 6. Comparison of the ${}^1A_1 \rightarrow {}^1T_2$ ($1s \rightarrow 2e^*$) transition energies measured using O K-edge XAS (STXM) and the energy of the ${}^1A_1 \rightarrow {}^1T_2$ ($\text{HOMO} \rightarrow 2e^*$) ligand-to-metal charge transfer (LMCT) bands measured using UV–visible spectroscopy.²⁷ A linear polynomial fit to the data (dashed line) gives the equation $y = (526.9 \pm 0.1) + (0.81 \pm 0.02)x$ with a correlation coefficient $r^2 = 0.996$.

changes in O 2p character for the empty e^* (π^*) and t_2^* ($\sigma^* + \pi^*$) orbitals of MO_4^- and MO_4^{2-} . It is instructive to begin by discussing bonding trends derived from the STXM O K-edge XAS measurements, which were made on all six MO_4^- and MO_4^{2-} anions. The first low-energy pre-edge peak, which was assigned to the O $1s \rightarrow e^*$ transition, shows a wide range of intensities for the complexes in Group 6 [CrO_4^{2-} , 1.9(2); MoO_4^{2-} , 2.7(3); WO_4^{2-} , 3.9(4)] and Group 7 [MnO_4^- , 2.9(3); TcO_4^- , 3.1(3); ReO_4^- , 4.2(4)] (Table 1). These data reveal that greater intensities (more mixing) are correlated to larger atomic numbers within a given group triad ($\text{Cr} < \text{Mo} < \text{W}$ and $\text{Mn} \cong \text{Tc} < \text{Re}$). In addition, the intensity for this $1s \rightarrow e^*$ feature increases on moving from Group 6 to Group 7 ($\text{Mn} > \text{Cr}$, $\text{Tc} > \text{Mo}$, $\text{Re} \approx \text{W}$). The increases in peak intensity can be substantial (by a factor of 1.1–1.5), suggesting that the amount of O 2p mixing with the d orbitals of e symmetry is appreciably larger for heavier metals. For O $1s \rightarrow t_2^*$ transitions, systematic increases in transition intensity with increasing atomic number in an individual group triad were not observed. For example, the intensities do not vary significantly for complexes with Group 6 metals [CrO_4^{2-} , 3.4(3); MoO_4^{2-} , 3.2(3); WO_4^{2-} , 3.6(4)] or Group 7 metals [MnO_4^- , 5.3(5); TcO_4^- , 4.4(4); ReO_4^- , 5.7(6)]. However, as observed for the O $1s \rightarrow e^*$ (π^*) transition, the O $1s \rightarrow t_2^*$ transition intensities increase substantially when moving from Group 6 MO_4^{2-} to Group 7 MO_4^- ($\text{Mn} > \text{Cr}$, $\text{Tc} > \text{Mo}$, $\text{Re} > \text{W}$).

The intensities measured in transmission using the STXM reflect a complex pattern of σ - and π -type mixing between oxygen 2p and metal d orbitals for different MO_4^{2-} and MO_4^- anions. Intensities measured using NIXS for ReO_4^- and the Group 6 MO_4^{2-} were compared to support these measurements, which showed that periodic trends in intensity are similar for both the transmission and NIXS measurements.³² In general, peak intensities for MO_4^{2-} and MO_4^- measured using NIXS are identical to those measured using transmission detection within one equivalent of the error (1σ). Larger deviations of 2σ were observed between the two measurements for both pre-edge peaks in the CrO_4^{2-} spectrum and for the low-energy pre-edge peak for MoO_4^{2-} . Because NIXS measurements at the O K-edge are immune to saturation effects,³² this may be evidence of small errors in the transmission data. However, the overall periodic trends in intensity described above are similar for both the transmission and NIXS

measurements. Relative MO_4^{2-} and MO_4^- experimental pre-edge peak intensities are also in good agreement with the oscillator strengths calculated using TD-DFT (Table 1). As observed experimentally, the TD-DFT shows a substantial increase in the intensity of the low-energy O $1s \rightarrow e^*$ (π^*) transition when descending individual Group triads (CrO_4^{2-} , 2.9; MoO_4^{2-} , 3.5; WO_4^{2-} , 3.9 and MnO_4^- , 3.7; TcO_4^- , 4.0; ReO_4^- , 4.2). A subtle decrease in intensity was calculated for the higher energy O $1s \rightarrow t_2^*$ ($\sigma^* + \pi^*$) transition, whether the metal is in Group 6 (CrO_4^{2-} , 3.4; MoO_4^{2-} , 3.2; WO_4^{2-} , 2.7) or in Group 7 (MnO_4^- , 4.3; TcO_4^- , 3.9; ReO_4^- , 3.7), as observed experimentally.

Oxygen K-edge transition intensities provided from the transmission XAS, NIXS, and TD-DFT measurements all support a consistent picture of the excited state electronic structure changes between MO_4^{2-} and MO_4^- anions (Figure 7). Intensities associated with the transitions into both e^* or t_2^*

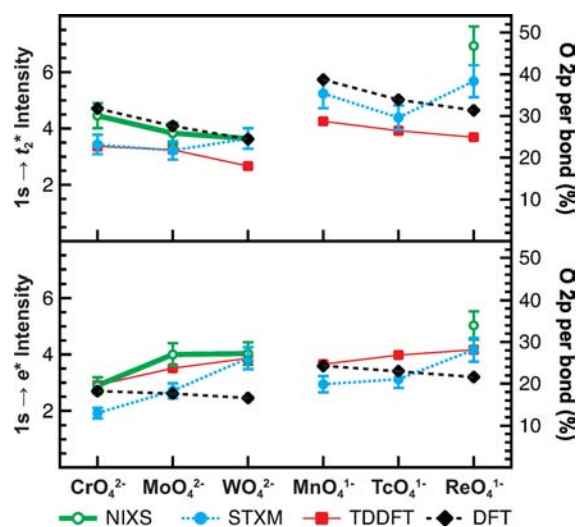


Figure 7. Comparison between the experimental (NIXS and STXM), calculated transition intensities (TD-DFT), and amount of O 2p character calculated by ground-state DFT (%), right axis). Intensities and O 2p character per bond values are separated into two plots involving the t_2^* (top) and e^* components (bottom).

orbitals increase moving right and down in the periodic table, such that the amount of O 2p and M d orbital mixing is greatest for ReO_4^- and smallest for CrO_4^{2-} . These changes in mixing are also loosely correlated with the strength of the ligand field dictated by the four oxo ligands (Δ_l) as estimated by the splitting of the O $1s \rightarrow e^*$ and O $1s \rightarrow t_2^*$ transitions. For example, the experimental e^* and t_2^* peak splittings measured for Group 7 MO_4^- increase by approximately 0.7 eV from MnO_4^- to ReO_4^- (Table 1). Experimental and TD-DFT peak splittings also increase generally when moving from Group 6 (MoO_4^{2-} and WO_4^{2-}) to Group 7 (TcO_4^- and ReO_4^-). Little or no change was observed between CrO_4^{2-} and MnO_4^- , which is consistent with the $e^* \rightarrow t_2^*$ (${}^2E \rightarrow {}^2T_2$) transition energies²⁷ observed for $d^1 \text{CrO}_4^{3-}$ (1.99 eV) and $d^1 \text{MnO}_4^{3-}$ (2.05 eV) via UV–visible spectroscopy.

The experimental and TD-DFT calculated O K-edge transition intensities and peak splittings correlate well with the trend of O 2p orbital mixing coefficients obtained from the virtual Kohn–Sham orbitals in the ground-state DFT calculation, as described at the beginning of the Results and Discussion (see also Figure 7 and Table S1 in the Supporting

Information). For example, the ground-state DFT calculations also show that the amount of O 2p mixing with the M d orbitals of both e^* (π^*) and t_2^* ($\sigma^* + \pi^*$) symmetry increases when moving from Group 6 MO_4^{2-} to Group 7 MO_4^- . The ground-state DFT calculations subtly differ in that they show a small decrease in O 2p character for the t_2^* ($\sigma^* + \pi^*$) orbitals when moving from first to second to third row transition metals for both the MO_4^{2-} and MO_4^- anions, while the experimental and TD-DFT results showed no change or only slight increases in O 2p character. The ground-state DFT calculations are considerably divergent in that they predict a minor decrease in O 2p character for the e^* (π^*) orbitals with heavier metals, while the experimental and TD-DFT clearly support the opposite trend. Hence, virtual orbital compositions obtained from the Mulliken populations in the ground-state DFT calculation do not provide an accurate representation of the excited state electronic structure in this case. In addition, spin-orbit coupling may contribute to additional mixing with the O 2p orbitals,^{33,34,55} which has not been taken into consideration by these hybrid DFT calculations, but is the focus of ongoing theoretical efforts.

CONCLUSION

These experimental and theoretical results provide insight into periodic trends in electronic structure and orbital mixing for metal–oxo multiple bonds, and demonstrate a spectroscopic approach that may be useful for studying metal–ligand multiple bonds involving metals and light atoms such as carbon, nitrogen or fluorine. The O K-edge spectra and DFT results show substantial variability in the extent of M–O mixing for the antibonding e^* (π^*) and t_2^* ($\sigma^* + \pi^*$) orbitals of tetrahedral d-block MO_4^{x-} anions. The NIXS, XAS, and TD-DFT results indicate that metal d and oxygen 2p orbital mixing increases by a factor of 1.1–1.5 in the e^* orbitals, and by a factor of 1.2–2.0 in the t_2^* orbitals, on traversing from Group 6 to Group 7. Within group triads, a pronounced increase in O 2p mixing by a factor of up to 2.0 is observed for the π -type antibonding interactions in the e^* orbitals on moving to heavier second and third row transition metals. Conversely, mixing in the t_2^* ($\sigma^* + \pi^*$) orbitals, on average, does not appreciably change on moving from 3d to 5d transition metals in either Group 6 or Group 7.

A simple theoretical framework to rationalize these experimental results can be derived from first-order perturbation theory, which establishes that orbital mixing is directly related to the spatial overlap between valence atomic orbitals and inversely proportional to their energy separation.⁵⁶ In an individual Group triad, O 2p mixing may increase through better spatial overlap with larger 4d and 5d atomic orbitals, but the 3d atomic orbitals will have the most favorable energy match. For example, the increase in π -type mixing in the antibonding e^* orbitals observed for the second and third row transition metals is indicative of improved π spatial overlap between the O 2p and more diffuse 4d and 5d atomic orbitals. Mixing in the t_2^* orbitals is extensive, even for CrO_4^{2-} and MnO_4^{2-} , and can be attributed to improved spatial overlap arising from more directional σ bonding character in the t_2^* orbitals (Figure 1). However, an increase in t_2^* mixing is not observed with second and third row transition metals, suggesting that improvements in spatial overlap in the bonding and antibonding t_2 orbitals are more effectively offset by an increasing energy mismatch between the O 2p and M 4d and 5d atomic orbitals. An increase in mixing is observed in both

the e^* and t_2^* orbitals on moving from Group 6 to Group 7. This increase in O 2p character may result from a stabilization of the d orbitals that occurs with increased metal charge, which facilitates orbital mixing by decreasing the energy mismatch with the O 2p orbitals.

These experimental and theoretical results provide a new illustration of the challenges associated with using formal bond orders to evaluate metal–ligand multiple bonding. Models of metal–oxo electronic structure should not rely solely on periodic changes in either d orbital energy or radial extension. On the contrary, orbital composition is influenced by a complex interplay between both factors, leading to changes in the energy and composition of the frontier orbitals even for formally isoelectronic metal oxos. Future efforts will be focused on evaluating relative changes in mixing with increases in d-electron count for the tetragonal metal monooxo and trans-dioxo compounds of d- and f-block metals.

EXPERIMENTAL SECTION

Sample Preparation. Reagents were obtained from commercial sources, purified by crystallization from H_2O , dried, and subsequently handled with rigorous exclusion of air and moisture using standard Schlenk, glovebox, and glovebag techniques to ensure that trace water or oxygen impurities were removed. For example, crystalline Na_2CrO_4 , K_2CrO_4 , Na_2MoO_4 , Na_2WO_4 , and NaReO_4 were ground in a mortar and pestle and heated (150 °C) under vacuum (10^{-3} Torr) for 24 h. Crystalline KMnO_4 was ground in a mortar and pestle and dried for several weeks under vacuum (10^{-3} Torr) in the presence of anhydrous CaSO_4 . $(\text{Ph}_4\text{P})\text{TcO}_4$ was prepared by adding a solution of pertechnetic acid (0.100 mL, 0.10 M, 0.010 mmol) in water to $\text{Ph}_4\text{P}\text{Cl}$ (0.020 g, 0.053 mmol) in water (0.9 mL). The resulting white precipitate was isolated by centrifugation, washed with water (1 mL), and dried at 95 °C overnight. Samples for FY, STXM, and NIXS measurements were prepared as previously described.³²

O K-Edge XAS Measurements. XAS spectra for the MO_4^{x-} anions were collected in transmission mode using the STXM at the Advanced Light Source-Molecular Environmental Sciences (ALS-MES) elliptically polarizing undulator beamline 11.0.2.³² For KMnO_4 , radiation damage occurred unless data acquisitions were limited to less than 5 min, which was achieved by reducing the dwell time (0.5 ms), increasing the step size (0.25 eV), and selecting particles larger than $4 \mu\text{m}^2$ in the dimensions perpendicular to the incident beam and thinner than ca. 100 nm in the dimension parallel to the incident beam. The FY XAS spectra were collected on beamlines 8.2 and 10.1 at SSRL (top-off mode at 350 mA).³² These VUV beamlines are equipped with bending magnet (8.2) and wiggler (10.1) insertion devices and spherical grating monochromators (approximately 200–1600 eV). Spectra with reproducible peak intensities were obtained with step sizes of 0.07 eV over the rising edge, and only minimal effects from radiation damage were observed for KMnO_4 .

As described previously,³² NIXS measurements for NaReO_4 and Na_2WO_4 were taken using LERIX at the PNC/XOR 20-ID beamline of the APS, which is an undulator beamline equipped with a double-crystal Si(111) monochromator that provides a typical photon flux of approximately 10^{12} photons/s.⁵⁷ NIXS measurements for Na_2CrO_4 and Na_2MoO_4 were taken using the 40 crystal X-ray Raman spectrometer on the wiggler beamline 6.2 at SSRL⁵⁸ through the beamline's Si(311) double-crystal monochromator and under normal operational conditions for the SPEAR3 storage ring (incident beam flux of 2×10^{12} photons/s at approximately 10 keV; 350 mA). The energy resolution at the Si(660) reflection was approximately 500 meV. The FY, XAS, and NIXS data were modeled as previously described.³² Errors in intensity associated with each measurement were estimated at 5% for the FY data and 10% for the STXM and NIXS data, which is based on our ability to reproduce the data over multiple experiments.³²

Electronic Structure Calculations and Simulated O K-Edge Spectra. Ground-state electronic structure calculations were

performed on MO_4^- and MO_4^{2-} species using the B3LYP hybrid density functional theory (DFT)^{59,60} in the Gaussian 09 code.⁶¹ The transition metals were modeled with the Stuttgart relativistic effective core potential (ecp) and basis set^{62,63} with the most diffuse s, p, and d functions removed. O was modeled using a Pople style double- ζ 6-31G(d',p') basis set with polarization functions optimized for heavy atoms.⁶⁴ These functionals and basis sets have demonstrated good agreement between experimental and simulated ligand K-edge XAS for organometallic and inorganic systems.^{32,37,40,65} The molecular orbital compositions of each compound were obtained by Mulliken population analysis of the individual molecular orbitals.

The O K-edge X-ray absorption spectra were simulated using TD-DFT. This approach has been applied successfully to simulate spectra for several other transition metal systems^{37,38,45–47} and to simulate the absorption spectrum of permanganate.⁴⁸ These calculations were conducted as described previously.^{32,37,38} A moderate energy shift (Table S2, Supporting Information) was established by setting the energy of transitions simulated for the d orbitals of e symmetry to be equal to those in the transmission XAS obtained using STXM, which accounts for the omission of the electronic relaxation associated with the core excitation, relativistic stabilization, and errors associated with the functional.³⁷ Calculated intensities were taken from the TD-DFT oscillator strengths and scaled to the O 1s \rightarrow e* transition in the O K-edge XAS (STXM) of ReO_4^- by applying a scaling factor of 86.2.

■ ASSOCIATED CONTENT

■ Supporting Information

Additional X-ray absorption spectra and calculated atomic compositions; complete refs 44 and 61. This material is available free of charge via the Internet at <http://pubs.acs.org>.

■ AUTHOR INFORMATION

Corresponding Author

erb@lanl.gov; stosh@lanl.gov; rlmartin@lanl.gov; dkshuh@lbl.gov

Notes

The authors declare no competing financial interest.

■ ACKNOWLEDGMENTS

This work was supported under the Heavy Element Chemistry Program at Los Alamos National Laboratory (LANL) by the Division of Chemical Sciences, Geosciences, and Biosciences, Office of Basic Energy Sciences, U.S. Department of Energy (DOE). LANL is operated by Los Alamos National Security, LLC, for the National Nuclear Security Administration of the DOE under contract DE-AC52-06NA25396. This work was also supported by the Director, DOE Office of Science, Office of Basic Energy Sciences, Division of Chemical Sciences, Geosciences, and Biosciences, at Lawrence Berkeley National Laboratory under contract DE-AC02-05CH11231. In addition, support was provided to LANL by Glenn T. Seaborg Institute Graduate and Postdoctoral Fellowships (S.G.M., S.R.D., J.A.B., P.Y.) and Director's Postdoctoral Fellowships (J.M.K.). Work at the University of Washington (G.T.S.) was supported by the DOE, Office of Basic Energy Sciences. The Advanced Light Source (ALS) is a national user facility supported by the DOE Office of Science, Office of Basic Energy Sciences (contract DE-AC02-05CH11231). PNC/XOR facilities at the Advanced Photon Source (APS), and research at these facilities was supported by the DOE, Office of Basic Energy Sciences, a Major Resources Support grant from NSERC, the University of Washington, Simon Fraser University, and the APS. Use of the APS was also supported by the DOE Office of Science, Office of Basic Energy Sciences at Argonne National Laboratory (contract DE-AC02-06CH11357). Portions of this research

were carried out at the Stanford Synchrotron Radiation Lightsource, a Directorate of SLAC National Accelerator Laboratory and an Office of Science User Facility operated for the DOE Office of Science by Stanford University. The SSRL Structural Molecular Biology Program is supported by the DOE Office of Biological and Environmental Research and by the National Institutes of Health, National Institute of General Medical Sciences (including P41GM103393) and the National Center for Research Resources (P41RR001209).

■ REFERENCES

- (1) Nugent, W. A.; Mayer, J. M. *Metal–Ligand Multiple Bonds*; John Wiley & Sons: New York, NY, 1988.
- (2) Holm, R. H. *Chem. Rev.* **1987**, *87*, 1401.
- (3) Kung, H. H. *Transition Metal Oxides: Surface Chemistry and Catalysis*; Elsevier: New York, 1989.
- (4) Fierro, J. L. G. *Metal Oxides*; CRC Press: New York, 2006.
- (5) Ferreira, K. N.; Iverson, T. M.; Maghlaoui, K.; Barber, J.; Iwata, S. *Science* **2004**, *303*, 1831.
- (6) Kaizer, J.; Klinker, E. J.; Oh, N. Y.; Rohde, J. U.; Song, W. J.; Stubna, A.; Kim, J.; Munck, E.; Nam, W.; Que, L. *J. Am. Chem. Soc.* **2004**, *126*, 472.
- (7) Yano, J.; Kern, J.; Sauer, K.; Latimer, M. J.; Pushkar, Y.; Biesiadka, J.; Loll, B.; Saenger, W.; Messinger, J.; Zouni, A.; Yachandra, V. K. *Science* **2006**, *314*, 821.
- (8) Que, L., Jr.; Tolman, W. B. *Nature* **2008**, *455*, 333.
- (9) Kanan, M. W.; Nocera, D. G. *Science* **2008**, *321*, 1072.
- (10) Ortiz de Montellano, P. R. *Chem. Rev.* **2010**, *110*, 932.
- (11) Karunadasa, H. I.; Chang, C. J.; Long, J. R. *Nature* **2010**, *464*, 1329.
- (12) Prat, I.; Mathieson, J. S.; Gueell, M.; Ribas, X.; Luis, J. M.; Cronin, L.; Costas, M. *Nat. Chem.* **2011**, *3*, 788.
- (13) Borovik, A. S. *Chem. Soc. Rev.* **2011**, *40*, 1870.
- (14) Sarma, R.; Angeles-Boza, A. M.; Brinkley, D. W.; Roth, J. P. *J. Am. Chem. Soc.* **2012**, *134*, 15371.
- (15) Griffith, W. P.; Wickins, T. D. *J. Chem. Soc. A* **1968**, 400.
- (16) Griffith, W. P. *J. Chem. Soc. A* **1969**, 211.
- (17) Mingos, D. M. P. *J. Organomet. Chem.* **1979**, *179*, C29.
- (18) Jorgensen, K. A.; Hoffmann, R. *J. Am. Chem. Soc.* **1986**, *108*, 1867.
- (19) $^{99\text{m}}\text{Tc}$ used in nuclear medicine is most commonly purified from ^{99}Mo , and isolated as TcO_4^- using the column chromatography concept developed at Brookhaven National Laboratory: Burdett, J. K. *Struct. Bonding (Berlin)* **1987**, *65*, 29.
- (20) Mayer, J. M. *Inorg. Chem.* **1988**, *27*, 3899.
- (21) Demachy, I.; Jean, Y. *Inorg. Chem.* **1997**, *36*, 5956.
- (22) Hummel, P.; Winkler, J. R.; Gray, H. B. *Dalton Trans.* **2006**, 168.
- (23) Winkler, J. R.; Gray, H. B. *Struct. Bonding (Berlin)* **2012**, *142*, 17.
- (24) Solomon, E. I.; Hedman, B.; Hodgson, K. O.; Dey, A.; Szilagyi, R. K. *Coord. Chem. Rev.* **2005**, *249*, 97.
- (25) Connor, J. A.; Ebsworth, E. A. V. *Adv. Inorg. Chem.* **1964**, *6*, 279.
- (26) Wolfsberg, M.; Helmholz, L. *J. Chem. Phys.* **1952**, *20*, 837.
- (27) Viste, A.; Gray, H. B. *Inorg. Chem.* **1964**, *3*, 1113.
- (28) Schroder, M. *Chem. Rev.* **1980**, *80*, 187.
- (29) Veldkamp, A.; Frenking, G. *J. Am. Chem. Soc.* **1994**, *116*, 4937.
- (30) Richards, P.; Tucker, W. D.; Srivastava, S. C. *Int. J. Appl. Radiat. Isot.* **1982**, *33*, 793.
- (31) See Long, K. M.; Goff, G. S.; Ware, S. D.; Jarvinen, G. D.; Runde, W. H. *Ind. Eng. Chem. Res.* **2012**, *51*, 10445 and references therein.
- (32) Bradley, J. A.; Yang, P.; Batista, E. R.; Boland, K. S.; Burns, C. J.; Clark, D. L.; Conradson, S. D.; Kozimor, S. A.; Martin, R. L.; Seidler, G. T.; Scott, B. L.; Shuh, D. K.; Tyliszczak, T.; Wilkerson, M. P.; Wolfsberg, L. E. *J. Am. Chem. Soc.* **2010**, *132*, 13914.
- (33) Green, J. C.; Kaltsoyannis, N.; Sze, K. H.; Macdonald, M. A. *Chem. Phys. Lett.* **1990**, *175*, 359.
- (34) Ziegler, T.; Rauk, A.; Baerends, E. J. *Chem. Phys.* **1976**, *16*, 209.

- (35) Stückl, A. C.; Daul, C. A.; Güdel, H. U. *J. Chem. Phys.* **1997**, *107*, 4606.
- (36) Shadle, S. E.; Hedman, B.; Hodgson, K. O.; Solomon, E. I. *J. Am. Chem. Soc.* **1995**, *117*, 2259.
- (37) Kozimor, S. A.; Yang, P.; Batista, E. R.; Boland, K. S.; Burns, C. J.; Clark, D. L.; Conradson, S. D.; Martin, R. L.; Wilkerson, M. P.; Wolfsberg, L. E. *J. Am. Chem. Soc.* **2009**, *131*, 12125.
- (38) Kozimor, S. A.; Yang, P.; Batista, E. R.; Boland, K. S.; Burns, C. J.; Christensen, C. N.; Clark, D. L.; Conradson, S. D.; Hay, P. J.; Lezama, J. S.; Martin, R. L.; Schwarz, D. E.; Wilkerson, M. P.; Wolfsberg, L. E. *Inorg. Chem.* **2008**, *47*, 5365.
- (39) Ray, K.; George, S. D.; Solomon, E. I.; Wieghardt, K.; Neese, F. *Chem.—Eur. J.* **2007**, *13*, 2783.
- (40) Minasian, S. G.; Kieth, J. M.; Batista, E. R.; Boland, K. S.; Christensen, C. N.; Clark, D. L.; Conradson, S. D.; Kozimor, S. A.; Martin, R. L.; Schwarz, D. E.; Shuh, D. K.; Wagner, G. L.; Wilkerson, M. P.; Wolfsberg, L. E.; Yang, P. *J. Am. Chem. Soc.* **2012**, *134*, 5586.
- (41) Bergmann, U.; Glatzel, P.; Cramer, S. P. *Microchem. J.* **2002**, *71*, 221.
- (42) Soininen, J. A.; Ankudinov, A. L.; Rehr, J. J. *Phys. Rev. B* **2005**, *72*, 045136.
- (43) Schuelke, W. *Electron Dynamics by Inelastic Scattering*; Oxford University Press: New York, 2007.
- (44) Bluhm, H.; et al. *J. Electron Spectrosc. Relat. Phenom.* **2006**, *150*, 86.
- (45) George, S. D.; Brant, P.; Solomon, E. I. *J. Am. Chem. Soc.* **2005**, *127*, 667.
- (46) Casarin, M.; Finetti, P.; Vittadini, A.; Wang, F.; Ziegler, T. *J. Phys. Chem. A* **2007**, *111*, 5270.
- (47) George, S. D.; Petrenko, T.; Neese, F. *Inorg. Chim. Acta* **2008**, *361*, 965.
- (48) Neugebauer, J.; Baerends, E. J.; Nooijen, M. *J. Phys. Chem. A* **2005**, *109*, 1168.
- (49) Martin, R. L.; Shirley, D. A. *Many-electron theory of photoemission. Electron Spectroscopy, Theory, Techniques and Applications*; Academic Press: New York, 1977; Vol. 1.
- (50) Segala, M.; Chong, D. P. *J. Electron Spectrosc. Relat. Phenom.* **2010**, *182*, 141.
- (51) Fillaux, C.; Guillaumont, D.; Berthet, J.-C.; Copping, R.; Shuh, D. K.; Tyliczszak, T.; Den Auwer, C. *Phys. Chem. Chem. Phys.* **2010**, *12*, 14253.
- (52) Wen, A. T.; Hitchcock, A. P. *Can. J. Chem.* **1993**, *71*, 1632.
- (53) Lancaster, K. M.; Finkelstein, K. D.; DeBeer, S. *Inorg. Chem.* **2011**, *50*, 6767.
- (54) Green, J. C.; Guest, M. F.; Hillier, I. H.; Jarrettsprague, S. A.; Kaltsoyannis, N.; Macdonald, M. A.; Sze, K. H. *Inorg. Chem.* **1992**, *31*, 1588.
- (55) Bursten, B. E.; Green, J. C.; Kaltsoyannis, N. *Inorg. Chem.* **1994**, *33*, 2315.
- (56) Albright, T. A.; Burdett, J. K.; Whangbo, M. *Orbital Interactions in Chemistry*; John Wiley and Sons: New York, 1985.
- (57) Fister, T. T.; Seidler, G. T.; Wharton, L.; Battle, A. R.; Ellis, T. B.; Cross, J. O.; Macrander, A. T.; Elam, W. T.; Tyson, T. A.; Qian, Q. *Rev. Sci. Instrum.* **2006**, *77*, 063901.
- (58) Sokaras, D.; Nordlund, D.; Weng, T. C.; Mori, R. A.; Velikov, P.; Wenger, D.; Garachtchenko, A.; George, M.; Borzenets, V.; Johnson, B.; Qian, Q.; Rabedeau, T.; Bergmann, U. *Rev. Sci. Instrum.* **2012**, *83*, 043112.
- (59) Becke, A. D. *J. Chem. Phys.* **1993**, *98*, 5648.
- (60) Lee, C. T.; Yang, W. T.; Parr, R. G. *Phys. Rev. B* **1988**, *37*, 785.
- (61) Frisch, M. J.; et al. *Gaussian 09*, Revision B.01; Gaussian Inc.: Wallingford, CT, 2009.
- (62) Dolg, M.; Wedig, U.; Stoll, H.; Preuss, H. *J. Chem. Phys.* **1987**, *86*, 866.
- (63) Andrae, D.; Haussermann, U.; Dolg, M.; Stoll, H.; Preuss, H. *Theo. Chim. Acta* **1990**, *77*, 123.
- (64) Petersson, G. A.; Bennett, A.; Tensfeldt, T. G.; Allaham, M. A.; Shirley, W. A.; Mantzaris, J. *J. Chem. Phys.* **1988**, *89*, 2193.
- (65) Daly, S. R.; Keith, J. M.; Batista, E. R.; Boland, K. S.; Clark, D. L.; Kozimor, S. A.; Martin, R. L. *J. Am. Chem. Soc.* **2012**, *134*, 14408.